

Global electromagnetic turbulence simulations of W7-X-like plasmas with GENE-3D

Felix Wilms^{1,†}, Alejandro Bañón Navarro¹, Gabriele Merlo²,
Leonhard Leppin¹, Tobias Görler¹, Tilman Dannert³,
Florian Hindenlang¹ and Frank Jenko¹

¹Max Planck Institute for Plasma Physics, Boltzmannstr. 2, 85748 Garching, Germany

²Oden Institute for Computational Engineering and Sciences, The University of Texas at Austin, Austin, TX 78712, USA

³Max Planck Computing and Data Facility, Giessenbachstr. 2, 85748 Garching, Germany

(Received 30 July 2021; revised 17 October 2021; accepted 19 October 2021)

The GENE-3D code, the global stellarator version of the established GENE framework, has been extended to an electromagnetic gyrokinetic code. This paper outlines the basic structure of the algorithm, highlighting the treatment of the electromagnetic terms. The numerical implementation is verified against the radially global GENE code in linear and nonlinear tokamak simulations, recovering excellent agreement between both codes. As a first application to stellarator plasmas, linear and nonlinear global simulations with kinetic electrons of ion temperature gradient (ITG) turbulence in Wendelstein 7-X were performed, showing a decrease of ITG activity through the introduction of electromagnetic effects via a finite plasma- β . The upgrade makes it possible to study a large variety of new physical scenarios, including kinetic electron and electromagnetic effects, reducing the gap between gyrokinetic models and physically realistic systems.

Key words: plasmas, turbulence simulation

1. Introduction

Wendelstein 7-X (W7-X) is the first stellarator that has been optimised for low neoclassical transport (Wolf 2008), besides other criteria. As such, it has been shown (Klinger *et al.* 2019) that turbulence has become the limiting factor in the confinement for a broad range of its experiments. In order to understand the inherently nonlinear nature of plasma turbulence, numerical simulations based on gyrokinetic theory have become indispensable (Garbet *et al.* 2010).

Using some of the world's most powerful supercomputers, it is possible nowadays to simulate gyrokinetic turbulence in stellarators globally, making it possible to take into account the full variation of the magnetic field on a flux surface while simultaneously considering its radial variations as well as temperature and density profiles – all of which are inherently impossible in flux-tube simulations. As such, studies like those of

† Email address for correspondence: felix.wilms@ipp.mpg.de

Navarro *et al.* (2020), Cole *et al.* (2020), Sánchez *et al.* (2020) and Wang *et al.* (2020) have paved the way in investigating ion temperature gradient (ITG) turbulence globally in stellarators.

However, while these results already are of high importance, all of them relied on an adiabatic electron model, where only the ions were treated as a gyrokinetic particle species. This model fails to address things like trapped electron mode turbulence or the interaction between trapped electrons and ion turbulence, as well as electromagnetic effects, something that can become important for high-density operation of fusion devices.

All of these considerations motivated the upgrade of GENE-3D (Maurer *et al.* 2020), the extension of the widely established GENE framework (Jenko *et al.* 2000) for three-dimensional magnetic field equilibria, to an electromagnetic gyrokinetic code, which is the focus of this work. In this paper, the underlying model of GENE-3D is presented, with special emphasis on the treatment of the electromagnetic terms in the gyrokinetic system of equations. Linear and nonlinear global verification studies using artificially heavy electrons to save computational cost against GENE are presented, showing excellent agreement between both codes, verifying the correctness and applicability of the electromagnetic upgrade. Finally, GENE-3D is used to perform global simulations of plasmas in W7-X with realistic electron mass and electromagnetic effects, something that, to the knowledge of the authors, has not been published before. It is found that, for the particular analytical background profiles used, the introduction of finite plasma- β leads to a reduction in linear as well as nonlinear ITG strength.

The rest of the paper is structured as follows. The GENE-3D framework is introduced in § 2, highlighting the gyrokinetic model it uses and the numerical methods to solve the corresponding set of equations. In § 3, results of verification studies of the code against the global version of GENE in linear and nonlinear, electromagnetic tokamak simulations are presented, testing the correctness of the numerical implementation. In § 4, the first global, nonlinear gyrokinetic simulations of W7-X incorporating kinetic electrons with realistic mass, as well as electromagnetic effects are discussed. Finally, the main results of this paper are summarised in § 5 and an outlook for future projects is given.

2. Extending GENE-3D to an electromagnetic code

This section focuses on the algorithmic details of the extension of GENE-3D to include effects of a perturbed parallel vector potential. First, a brief overview of the gyrokinetic system of equations is given in § 2.1, followed by details specific to the implementation in § 2.2. Finally, additional information about the numerics of the code is presented in Appendix A.

2.1. Gyrokinetic Vlasov–Maxwell system

The GENE-3D code is a Eulerian code that solves the gyrokinetic Vlasov equation, coupled to Maxwell’s equations (e.g. Brizard & Hahm 2007) on a five-dimensional grid in phase space, using two velocity dimensions – the velocity parallel to the equilibrium magnetic field v_{\parallel} and the magnetic moment $\mu = mv_{\perp}^2/2B_0$ – and three spatial dimensions (x, y, z), representing a field-aligned coordinate system (Beer, Cowley & Hammett 1995). Furthermore, it employs the so-called ‘ δf ’ splitting (e.g. Garbet *et al.* (2010), and references therein). In this approach, one assumes that the full gyrocentre distribution function F_{σ} of species σ can be split into a stationary background distribution function $F_{0,\sigma}$, describing the plasma at thermal equilibrium, and a time-dependent, first-order perturbation $F_{1,\sigma}$:

$$F_{\sigma} = F_{0,\sigma} + F_{1,\sigma}, \quad \text{with } \|F_{1,\sigma}\|/\|F_{0,\sigma}\| \sim O(\epsilon_{\delta}) \ll 1, \quad (2.1)$$

where ϵ_δ is a smallness parameter describing the scale relation between background and perturbed quantities. The GENE-3D code assumes that the background distribution is given by a local Maxwellian:

$$F_{0,\sigma} = F_{M,\sigma}(\mathbf{x}, v_{\parallel}, \mu) = \frac{n_{0,\sigma}(\mathbf{x})}{(\pi)^{3/2} v_{th,\sigma}(\mathbf{x})^3} \exp\left(-\frac{m_\sigma v_{\parallel}^2/2 + \mu B_0(\mathbf{x})}{T_{0,\sigma}(\mathbf{x})}\right). \quad (2.2)$$

Here, m_σ , $n_{0,\sigma}$ and $T_{0,\sigma}$ are the mass, equilibrium background density and temperature of particle species σ at position \mathbf{x} , respectively. Furthermore, B_0 gives the strength of the equilibrium magnetic field, v_{\parallel} and μ denote the velocity parallel to the magnetic field and the magnetic moment, respectively, and $v_{th,\sigma} = \sqrt{2T_{0,\sigma}(\mathbf{x})/m_\sigma}$ is the thermal velocity of particle species σ . Under this assumption, the gyrokinetic equation for particle species σ , including a perturbation of the parallel vector potential, can be written as

$$\begin{aligned} \frac{\partial F_{1,\sigma}}{\partial t} = & - [v_{\parallel} \mathbf{b}_0 + (\mathbf{v}_\chi + \mathbf{v}_{\nabla B} + \mathbf{v}_c)] \cdot \nabla F_{1,\sigma} + \frac{\mu}{m_\sigma} \mathbf{b}_0 \cdot \nabla B_0 \frac{\partial F_{1,\sigma}}{\partial v_{\parallel}} \\ & - \mathbf{v}_\chi \cdot \left[\nabla \ln(n_{0,\sigma}) + \nabla \ln(T_{0,\sigma}) \left(\frac{m_\sigma v_{\parallel}^2/2 + \mu B_0}{T_{0,\sigma}} - \frac{3}{2} \right) \right] F_{M,\sigma} \\ & - \frac{q_\sigma F_{M,\sigma}}{T_{0,\sigma}} [v_{\parallel} \mathbf{b}_0 + (\mathbf{v}_\chi + \mathbf{v}_{\nabla B} + \mathbf{v}_c)] \cdot \nabla \mathcal{G}\{\phi_1\} - \frac{q_\sigma v_{\parallel}}{c} \frac{F_{M,\sigma}}{T_{0,\sigma}} \frac{\partial \mathcal{G}\{A_{1,\parallel}\}}{\partial t} \\ & - (\mathbf{v}_{\nabla B} + \mathbf{v}_c) \cdot \left[\nabla \ln(n_{0,\sigma}) + \nabla \ln(T_{0,\sigma}) \left(\frac{m_\sigma v_{\parallel}^2/2 + \mu B_0}{T_{0,\sigma}} - \frac{3}{2} \right) \right] F_{M,\sigma} \\ & - \mathbf{v}_{E_0} \cdot \nabla F_{1,\sigma} + C[F_{1,\sigma}], \end{aligned} \quad (2.3)$$

where $\chi = \phi_1 - v_{\parallel} A_{1,\parallel}/c$ is called the gyrokinetic potential. The operator $\mathcal{G}\{\cdot\}$ defines the forward-gyroaverage operator

$$\mathcal{G}\{u\}(X) = \frac{1}{2\pi} \int_0^{2\pi} u(X + \mathbf{r}(\vartheta)) d\vartheta, \quad (2.4)$$

where X denotes the gyrocentre position and \mathbf{r} is the gyroradius vector orthogonal to the local magnetic field. The drift velocities appearing in (2.3) are defined as follows:

$$\left. \begin{aligned} \mathbf{v}_{E_0} &\equiv \frac{c}{B_0^2} \mathbf{B}_0 \times \nabla \phi_0, & \mathbf{v}_\chi &\equiv \frac{c}{B_0^2} \mathbf{B}_0 \times \nabla \mathcal{G}\{\chi\}, \\ \mathbf{v}_{\nabla B} &\equiv \frac{\mu c}{q_\sigma B_0^2} \mathbf{B}_0 \times \nabla B_0, & \mathbf{v}_c &\equiv \frac{v_{\parallel}^2}{\Omega_\sigma} \left(\mathbf{b}_0 \times \left(\nabla \ln(B_0) + \frac{\beta}{2} \nabla \ln(p_0) \right) \right), \end{aligned} \right\} \quad (2.5)$$

where $\Omega_\sigma = (q_\sigma B_0)/(m_\sigma c)$ is the gyrofrequency of species σ , $\mathbf{b}_0 = \mathbf{B}_0/B_0$ is the unit vector in the direction of the equilibrium magnetic field \mathbf{B}_0 , p_0 is the equilibrium thermodynamic pressure, $\beta = 8\pi p_0/B_0^2$ is the ratio between plasma pressure and magnetic field strength and c is the speed of light.

At the current stage, GENE-3D uses a linearised Landau–Boltzmann collision operator for $C[F_{1,\sigma}]$. Furthermore, the interplay between neoclassical and gyrokinetic physics is represented by the term coupling the curvature and ∇B drifts to the background

Maxwellian (Oberparleiter *et al.* 2016), and the effects of a long-wavelength, radial electric field on the system (Helander & Simakov 2008; Mishchenko & Kleiber 2012) are represented by the term proportional to v_{E_0} in (2.3). Though they are incorporated in the main algorithm, these effects are neglected in the simulations presented in this paper for simplicity.

The system is closed by the gyrokinetic field equations. Poisson's equation, providing the electrostatic potential, reads

$$\nabla^2 \phi_1(\mathbf{x}, t) \approx \nabla_{\perp}^2 \phi_1(\mathbf{x}, t) = -4\pi \sum_{\sigma} q_{\sigma} n_{1,\sigma}(\mathbf{x}, t), \quad (2.6)$$

where only the spatial derivatives perpendicular to the magnetic field are retained, which is in accordance with the gyrokinetic ordering. In order to calculate the density perturbation at the particle position \mathbf{x} from the gyrocentre position \mathbf{X} , GENE-3D employs a first-order pull-back transformation (e.g. Brizard & Hahm 2007):

$$n_{1,\sigma}(\mathbf{x}, t) = \int \mathcal{K}\{F_{1,\sigma}\} - \left(\frac{q_{\sigma} F_{M,\sigma}}{T_{0,\sigma}} \phi_1 - \mathcal{K} \left\{ \frac{q_{\sigma} F_{M,\sigma}}{T_{0,\sigma}} \mathcal{G}\{\phi_1\} \right\} \right) d^3v. \quad (2.7)$$

The operator $\mathcal{K}\{\cdot\}$ denotes the backward-gyroaverage operator, which is defined here as

$$\mathcal{K}\{u\}(\mathbf{x}) = \frac{1}{2\pi} \int_0^{2\pi} u(\mathbf{x} - \mathbf{r}(\vartheta)) d\vartheta. \quad (2.8)$$

Assuming a quasi-neutral limit ($\nabla_{\perp}^2 \phi_1 \approx 0$), Poisson's equation can be rewritten as

$$\sum_{\sigma} q_{\sigma}^2 \int \left(\frac{F_{M,\sigma}}{T_{0,\sigma}} \phi_1 - \mathcal{K} \left\{ \frac{F_{M,\sigma}}{T_{0,\sigma}} \mathcal{G}\{\phi_1\} \right\} \right) d^3v = \sum_{\sigma} q_{\sigma} \int \mathcal{K}\{F_{1,\sigma}\} d^3v. \quad (2.9)$$

At the current stage, magnetic compressibility, associated with a parallel perturbation of the magnetic field, is neglected, so that only the parallel vector potential $A_{1,\parallel}$ is retained in GENE-3D, which is determined by the parallel component of Ampere's law:

$$\nabla_{\perp}^2 A_{1,\parallel} = -\frac{4\pi}{c} \sum_{\sigma} j_{1,\parallel,\sigma} = -\frac{4\pi}{c} \sum_{\sigma} \int v_{\parallel} \mathcal{K}\{F_{1,\sigma}\} d^3v, \quad (2.10)$$

self-consistently with the gyrokinetic equation and Poisson's equation.

2.2. Electromagnetic model

Although (2.3), (2.9) and (2.10) are an analytically closed system, particular care has to be taken of the term containing the partial time derivative of $A_{1,\parallel}$ in (2.3). The approach used in GENE for a long time was to introduce a new distribution function $g_{\sigma} = F_{1,\sigma} + (q_{\sigma} v_{\parallel} F_{M,\sigma} A_{1,\parallel}) / (T_{0,\sigma} c)$ and solving the corresponding gyrokinetic system for g_{σ} instead of $F_{1,\sigma}$ (Görler *et al.* 2011). However, it was shown in Crandall (2019), that such a scheme becomes numerically unstable in nonlinear simulations at high plasma- β , although being stable linearly. In the same publication, an alternative scheme was proposed, similar to the one presented in Reynders (1993), which has been included in the standard version of

GENE recently. This scheme is also used in GENE-3D and is presented in the following. By defining the parallel inductive electric field as

$$E_{\parallel}^{\text{ind}} \equiv -\frac{1}{c} \frac{\partial A_{1,\parallel}}{\partial t}, \tag{2.11}$$

one can rewrite the gyrokinetic equation in the form

$$\frac{\partial F_{1,\sigma}}{\partial t} = R_{\sigma} + q_{\sigma} v_{\parallel} \frac{F_{M,\sigma}}{T_{0,\sigma}} \mathcal{G} \{E_{\parallel}^{\text{ind}}\}, \tag{2.12}$$

where the term R_{σ} contains all the contributions to the right-hand side of the gyrokinetic equation (2.3), except the one accounting for the parallel inductive electric field, and reads

$$\begin{aligned} R_{\sigma} = & - [v_{\parallel} \mathbf{b}_0 + (\mathbf{v}_{\nabla B} + \mathbf{v}_c)] \cdot \left(\nabla F_{1,\sigma} + \frac{q_{\sigma} F_{M,\sigma}}{T_{0,\sigma}} \nabla \mathcal{G} \{ \phi_1 \} \right) \\ & - \mathbf{v}_{\chi} \cdot \left(\nabla F_{1,\sigma} + \frac{q_{\sigma} F_{M,\sigma}}{T_{0,\sigma}} \nabla \mathcal{G} \{ \phi_1 \} \right) + \frac{\mu}{m_{\sigma}} \mathbf{b}_0 \cdot \nabla B_0 \frac{\partial F_{1,\sigma}}{\partial v_{\parallel}} \\ & - \mathbf{v}_{\chi} \cdot \left[\nabla \ln(n_{0,\sigma}) + \nabla \ln(T_{0,\sigma}) \left(\frac{m_{\sigma} v_{\parallel}^2 / 2 + \mu B_0}{T_{0,\sigma}} - \frac{3}{2} \right) \right] F_{M,\sigma} \\ & - (\mathbf{v}_{\nabla B} + \mathbf{v}_c) \cdot \left[\nabla \ln(n_{0,\sigma}) + \nabla \ln(T_{0,\sigma}) \left(\frac{m_{\sigma} v_{\parallel}^2 / 2 + \mu B_0}{T_{0,\sigma}} - \frac{3}{2} \right) \right] F_{M,\sigma} \\ & - \mathbf{v}_{E_0} \cdot \nabla F_{1,\sigma} + C[F_{1,\sigma}]. \end{aligned} \tag{2.13}$$

The next step is to take the partial time derivative of Ampere’s law (2.10) and multiply by $(-1/c)$:

$$-\frac{1}{c} \nabla_{\perp}^2 \frac{\partial A_{1,\parallel}}{\partial t} = \nabla_{\perp}^2 E_{\parallel}^{\text{ind}} = \frac{4\pi}{c^2} \sum_{\sigma} q_{\sigma} \int v_{\parallel} \mathcal{K} \left\{ \frac{\partial F_{1,\sigma}}{\partial t} \right\} d^3 v. \tag{2.14}$$

Inserting definition (2.12) into (2.14) eliminates the explicit coupling of the equation to the particle distribution function $F_{1,\sigma}$. Therefore, one obtains an equation that treats the inductive electric field as an independent electromagnetic field:

$$\nabla_{\perp}^2 E_{\parallel}^{\text{ind}} - \frac{4\pi}{c^2} \sum_{\sigma} q_{\sigma}^2 \int v_{\parallel}^2 \mathcal{K} \left\{ \frac{F_{M,\sigma}}{T_{0,\sigma}} \mathcal{G} \{ E_{\parallel}^{\text{ind}} \} \right\} d^3 v = \frac{4\pi}{c^2} \sum_{\sigma} q_{\sigma} \int v_{\parallel} \mathcal{K} \{ R_{\sigma} \} d^3 v. \tag{2.15}$$

Using (2.9), (2.10), (2.12), (2.13) and (2.15), the evolution of the distribution function $F_{1,\sigma}$ can be calculated by treating time as a discrete variable and using a numerical scheme to solve (2.12) in the above system approximately. For this, GENE-3D provides several explicit Runge–Kutta schemes, with a fourth-order-accurate Runge–Kutta scheme (RK4) being the default option.

3. Code verification

Having introduced the major changes performed to the GENE-3D code, the following subsections focus on comparing its results of global, electromagnetic tokamak simulations with those obtained from GENE. As the implementation of the electromagnetic terms in the gyrokinetic equation is independent of the field geometry, these cases provide a simple scenario for code validation. Benchmarks with other stellarator codes capable of performing electromagnetic simulations are left for future work.

3.1. Linear simulations with varying plasma- β

This subsection presents a linear verification study between GENE-3D and GENE over a large range of plasma pressures. For this, linear growth rates and mode frequencies of the most unstable mode are calculated varying the plasma- β and are compared with the results presented in Görler *et al.* (2016).

The geometry is a tokamak with circular, concentric flux surfaces, with a magnetic field strength of $B_0 = 2.0$ T on axis, which is called B_{ref} in the following, a major radius of $R_0 = 1.67$ m, an inverse aspect ratio of $a/R_0 = 0.36$ and a safety factor profile

$$q(x) = 0.86 - 0.16(x/a) + 2.52(x/a)^2. \quad (3.1)$$

Furthermore, density and temperature profiles are defined according to

$$\frac{A}{A(x_0)} = \exp \left[-\kappa_A w_A \frac{a}{R_0} \tanh \left(\frac{x - x_0}{w_A a} \right) \right] \quad (3.2)$$

for both electrons and ions, where $A = (n, T_i, T_e)$. The corresponding normalised gradients are

$$\frac{R_0}{L_A} = -R_0 \frac{\partial \ln(A)}{\partial x} = \kappa_A \cosh^{-2} \left(\frac{x - x_0}{w_A a} \right), \quad (3.3)$$

with $T(x_0) = 2.14$ keV, where $x_0/R_0 = 0.5$ is the position at which the gradients have their maximum. The density at position x_0 is adjusted to obtain the desired value of the reference plasma $\beta(x_0) = 8\pi n(x_0)T(x_0)/B_{\text{ref}}^2$. The parameters κ_A and w_A set the amplitude and the width of the gradients, respectively, and are chosen to be $\kappa_{T_i} = \kappa_{T_e} = 6.96$, $w_{T_i} = w_{T_e} = 0.3$, $\kappa_{n_i} = \kappa_{n_e} = 2.23$ and $w_{n_i} = w_{n_e} = 0.3$. The box lengths are chosen to be $(L_x, L_{v_{\parallel}}, L_{\mu}) = (80 \rho_s, 3 v_{\text{th},\sigma}, 9 T_{0,\sigma}(x_0)/B_{\text{ref}})$ and $L_y = 21.13 \rho_s$, which results in resolving multiples of the toroidal mode number $n_0 = 19$. Here, $\rho_s = c_s/\Omega_s$ is the ion sound Larmor radius at reference position x_0 . The simulation is performed using deuterium as ionic species, as well as electrons that have twice their realistic mass. The resolution at which GENE-3D converged is $(1344 \times 16 \times 16 \times 64 \times 32)$ in $(x, y, z, v_{\parallel}, \mu)$, respectively, and hyperdiffusion was set as $\eta_x = 2.0$, $\eta_y = 0.05$, $\eta_z = 2.0$ and $\eta_{v_{\parallel}} = 0.2$. As is mentioned in Appendix A, periodic boundary conditions are employed in the bi-normal direction, whereas zero-valued Dirichlet boundary conditions are used for the radial domain. In order to avoid numerical instabilities caused by the fixed boundaries, buffer zones with a Krook damping operator are used at the radial boundaries, each covering 5% of the domain.

Figure 1(a) shows the growth rate γ of the dominant linear instability as a function of β , whereas figure 1(b) shows the frequency ω of the respective mode. The red lines indicate the results obtained from GENE, whereas blue represents the results of GENE-3D. Excellent agreement is found for both frequencies and growth rates as the relative difference between the results of both codes is below 3% in all cases. In particular, one can observe the expected stabilisation of the ITG mode by increasing β for both codes, as the growth rate decreases for β between 0.5% and 1.4%, while the frequency changes only slightly in the same interval. For values of β between 1.4% and 1.75% one can observe a transition of dominant modes from an ITG mode to a kinetic ballooning mode (KBM), which can be identified by the rapid increase in the mode frequency. The results for this interval are only shown here for the GENE code, since resolving this transition requires a much higher resolution than the one that was already used, which makes it impractical to investigate it with GENE-3D. Increasing β further results in an

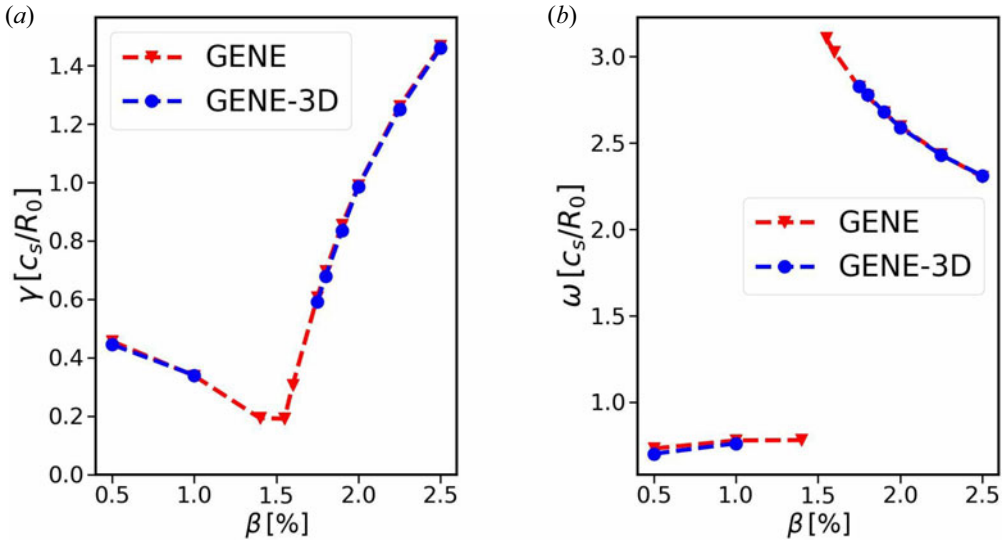


FIGURE 1. Linear growth rates (a) and mode frequencies (b) of the $n_0 = 19$ mode as a function of β . Red shows the results obtained from GENE, blue those from GENE-3D.

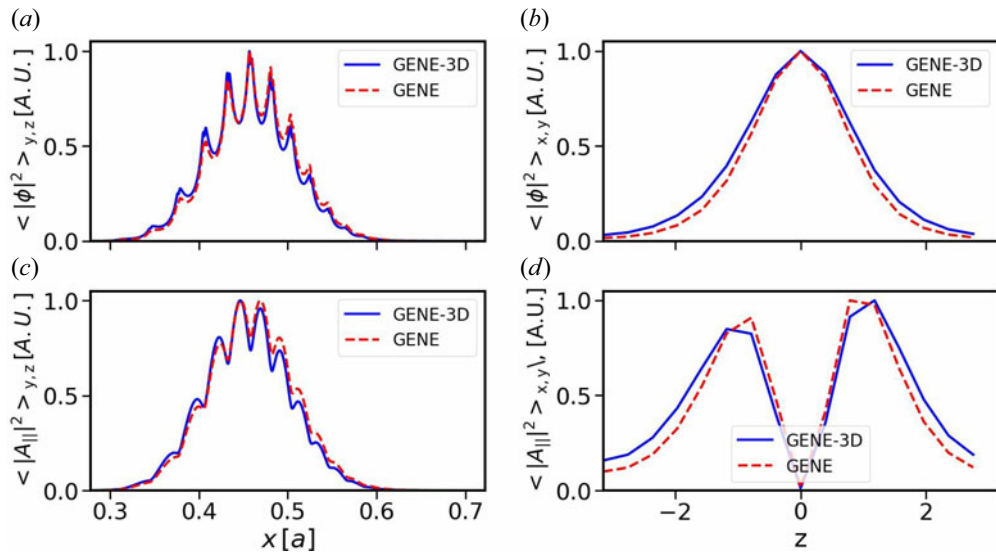


FIGURE 2. Normalised squares of the electrostatic and parallel vector potential for the scenario using $\beta = 2.5\%$. Radial (a) and poloidal (b) structures of the electrostatic potential, and radial (c) and poloidal (d) structures of the parallel vector potential. The red dashed line shows the results obtained from GENE, the blue solid line those from GENE-3D.

amplification of the KBM growth rate, while simultaneously causing a moderate decrease in its frequency, as observed with both codes. Finally, the radial and poloidal structures of the KBM at $\beta = 2.5\%$ are compared in figure 2, again showing excellent agreement between both codes.

3.2. Nonlinear turbulence at finite plasma-β in a tokamak

While the geometry being used is kept the same, it is beneficial for a nonlinear comparison to choose a broader profile than the one used in the previous subsection, as there is less unwanted profile relaxation in a gradient-driven approach with GENE-3D. Therefore, new plasma profiles of the form

$$\frac{A}{A(x_0)} = \left[\frac{\cosh\left(\frac{x - x_0 + \Delta_A}{w_A}\right)}{\cosh\left(\frac{x - x_0 - \Delta_A}{w_A}\right)} \right]^{-(\kappa_A w_A/2)(a/R_0)} \tag{3.4}$$

are chosen, with $x_0/R_0 = 0.5$, $\kappa_{T_i} = \kappa_{T_e} = 6.66$, $\kappa_n = 2.20$, $w_{T_i} = w_{T_e} = w_n = 0.04$ and $\Delta_{T_i} = \Delta_{T_e} = \Delta_n = 0.8$. Furthermore, the plasma pressure is such that $\beta_e(x_0) = 0.75\%$. In order to save computational time, the simulations were performed further increasing the electron-to-ion mass ratio to $m_e/m_i = 0.01$ and a finite-size parameter $\rho_s^* = \rho_s/L_{\text{ref}} = \rho_s/R_0 = 0.01$. The simulation covers the radial domain $0.1 \leq x/R_0 \leq 0.9$, using buffer zones of 10% at each side, with normalised box sizes being $(L_x, L_y, L_{v_{||}}, L_\mu) = (80.0 \rho_s, 111.4 \rho_s, 3 v_{\text{th},\sigma}, 9 T_{0,\sigma}(x_0)/B_{\text{ref}})$ and a resolution of $(n_x, n_{k_y}, n_z, n_{v_{||}}, n_\mu) = (160 \times 64 \times 24 \times 64 \times 24)$ for GENE and $(n_x, n_y, n_z, n_{v_{||}}, n_\mu) = (160 \times 256 \times 24 \times 64 \times 24)$ for GENE-3D. Finally, heat and particle sources, which are explained in Appendix A, were added with amplitudes being $\kappa_H = \kappa_P = 0.1$ and hyperdiffusion was set as $\eta_x = \eta_y = 0.05$, $\eta_z = 2.0$ and $\eta_{v_{||}} = 0.2$.

In order to compare the results of the two nonlinear simulations, the heat fluxes Q_σ for species σ are considered in the following. The heat flux itself can be split into an electrostatic and an electromagnetic component, $Q_\sigma = Q_{\text{es},\sigma} + Q_{\text{em},\sigma}$, which are defined as

$$\frac{Q_{\text{es},\sigma}}{Q_{\text{GB}}} = \frac{m_\sigma c}{2B_0^2} \int v^2 F_{1,\sigma}^{\text{particle}}(\mathbf{x}, \mathbf{v}, t) \mathbf{B}_0 \times \nabla \mathcal{G} \{\phi_1\} d^3 v \tag{3.5}$$

and

$$\frac{Q_{\text{em},\sigma}}{Q_{\text{GB}}} = -\frac{m_\sigma}{2c} \int v^2 F_{1,\sigma}^{\text{particle}}(\mathbf{x}, \mathbf{v}, t) v_{||} \nabla A_{1,||} \times \mathbf{b}_0 d^3 v, \tag{3.6}$$

respectively, with

$$Q_{\text{GB}} = n_{\text{ref}} T_{\text{ref}} c_s (\rho_s^*)^2. \tag{3.7}$$

Here, $F_{1,\sigma}^{\text{particle}}$ is the perturbed distribution function of species σ , evaluated at particle position.

Figure 3 shows the volume-averaged time traces of the ion and electron heat flux contributions. The fluxes are time-averaged over the interval $t \in [100, 345]R_0/c_s$, which roughly contains the same number of burst, as follows. The time traces are divided in disjoint intervals each approximately three autocorrelation times long. An average over each one of them is performed, the result of which is then used to compute an ensemble mean and variance of the heat flux. The results are presented in table 1. Both simulations are in good agreement with each other, as the relative difference between their respective ensemble mean values is below 10% for all components.

The radial profiles of the heat flux contributions, averaged over a flux surface and in time, shown in figure 4, recover reasonable agreement between both codes as well. Here GENE and GENE-3D produce similar heat flux profiles, where ion and electron contributions are comparable in their magnitude. For both particle species, the

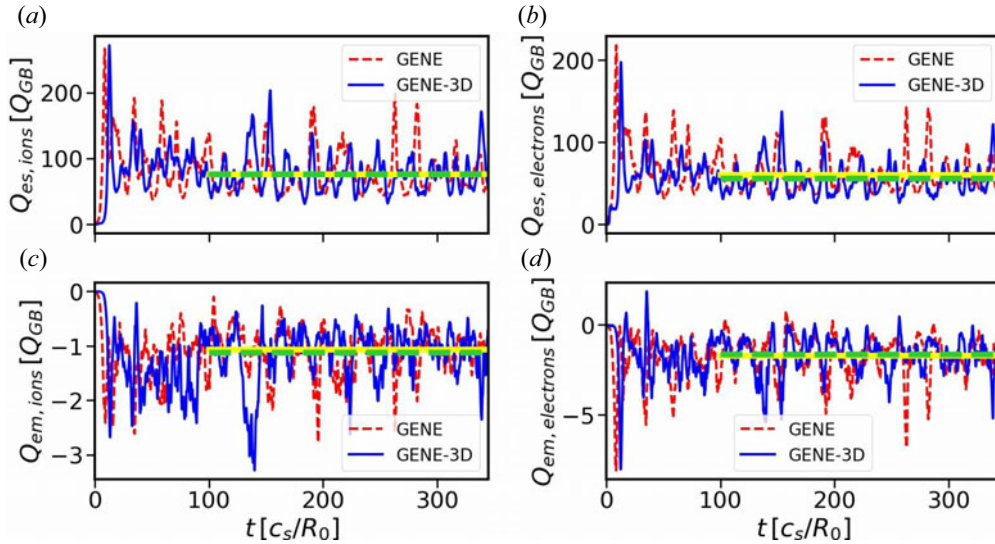


FIGURE 3. Time traces of the volume-averaged electron and ion heat fluxes. Yellow and green lines indicate average over the given time interval for GENE and GENE-3D, respectively. Electrostatic heat flux of ions (a) and electrons (b), and electromagnetic heat flux of ions (c) and electrons (d).

Heat flux [Q_{GB}]	GENE	GENE-3D
$Q_{es,ions}$	76 ± 7	75 ± 11
$Q_{es,electrons}$	60 ± 5	55 ± 6
$Q_{em,ions}$	-1.07 ± 0.13	-1.13 ± 0.15
$Q_{em,electrons}$	-1.70 ± 0.32	-1.65 ± 0.33

TABLE 1. Time-averaged heat flux contributions of GENE and GENE-3D.

fluxes are dominated by the electrostatic contribution, peaking around $x/R_0 = 0.6$. At this position, GENE calculates heat fluxes of $Q_{es,ions} = 103.24 Q_{GB}$ and $Q_{es,electrons} = 80.09 Q_{GB}$, whereas GENE-3D gives $Q_{es,ions} = 104.72 Q_{GB}$ and $Q_{es,electrons} = 75.41 Q_{GB}$. Both results differ by less than 6%, giving additional confidence in the numerical implementation of GENE-3D. Finally, the spectra of the electrostatic heat fluxes at $x/R_0 = 0.6$ are compared in figure 5. There are some small deviations between the heat flux spectra of both codes at the smallest scale, which is the result of the different representations of the bi-normal coordinate. Nevertheless, there is excellent agreement of the spectra in the wavenumber interval where most of the transport is located. Therefore, overall the linear as well as nonlinear verification studies of GENE-3D can be considered successful.

4. Electromagnetic effects on ITG turbulence in W7-X

Motivated by the successful verification in axisymmetric scenarios, electromagnetic simulations of W7-X are presented in this section. As the aim is to address the effect of finite plasma- β on ITG turbulence (Snyder & Hammett 2001) in W7-X, kinetic electron simulations in the electrostatic limit of $\beta_e(x_0) = 10^{-4}$ and electromagnetic simulations with $\beta_e(x_0) = 0.5\%$ were performed.

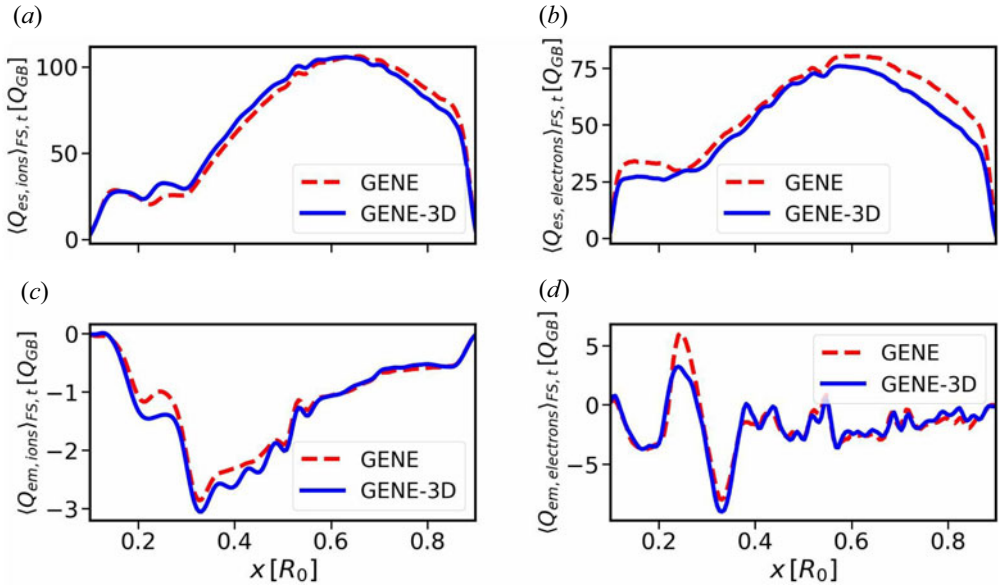


FIGURE 4. Radial profiles of heat flux contributions. Electrostatic heat flux of ions (a) and electrons (b), and electromagnetic heat flux of ions (c) and electrons (d).

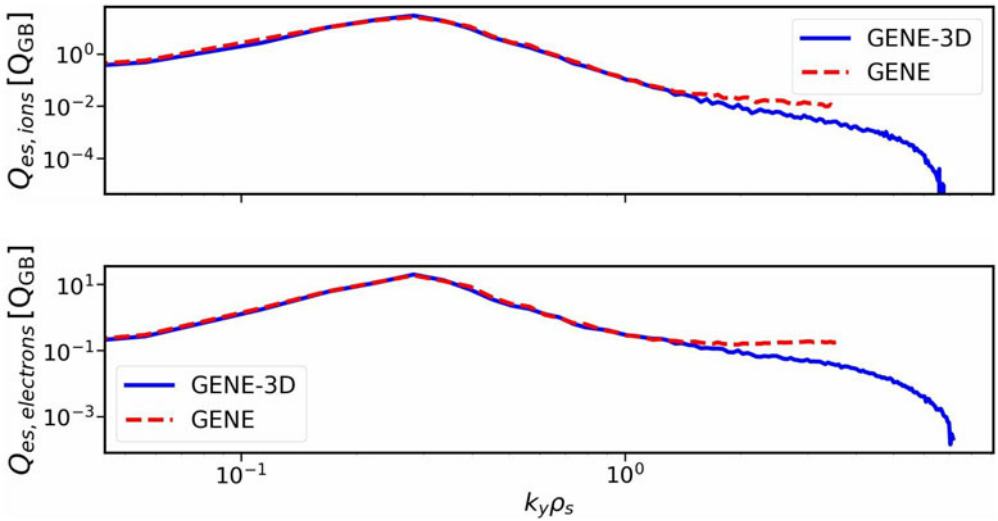


FIGURE 5. The k_y spectra of the electrostatic heat fluxes, evaluated at $x/R_0 = 0.6$.

The profiles shown in figure 6 were used for all simulations discussed in this section. The variation of plasma- β was achieved by varying the reference density n_{ref} . The specific choice of profiles localises turbulence in the centre of the plasma volume, such that one does not need to simulate the entire radial domain, with significant computational savings. The profiles are chosen to destabilise ITG modes by setting $\eta_i = L_n/L_{T_i} > 1$ and $\eta_e = L_n/L_{T_e} = 1$. The specific form of the profiles is given by (3.4), with the defining parameters set to $\kappa_{T_i} = 4.0$, $\kappa_{T_e} = 1.0$, $w_{T_i} = w_{T_e} = 0.04$, $\Delta_{T_i} = \Delta_{T_e} = 0.17$, $\kappa_n = 1.0$, $w_n = 0.04$ and $\Delta_n = 0.17$. For both cases, the standard configuration of W7-X was used,

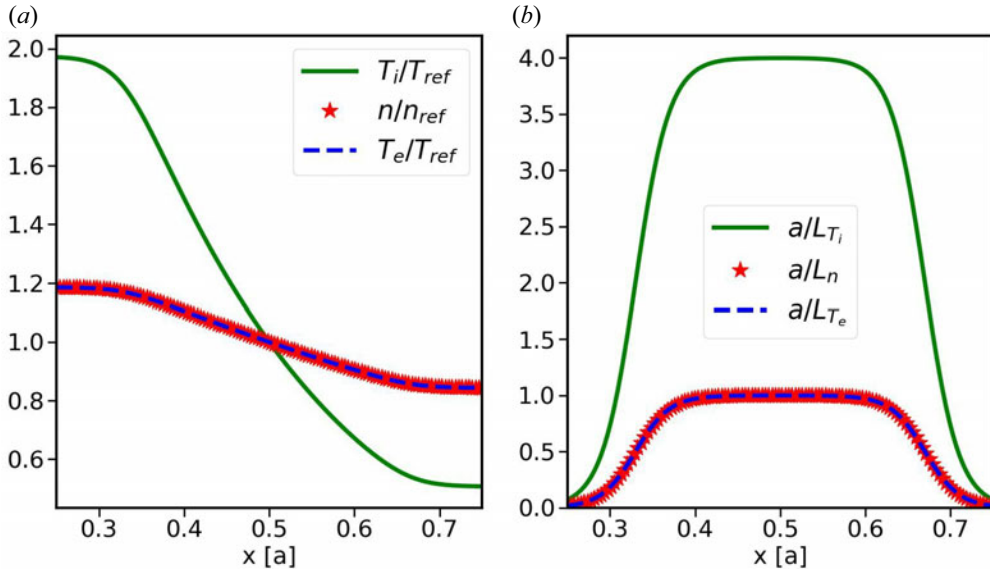


FIGURE 6. (a) Initial density and temperature profiles. (b) Initial density and temperature gradient profiles.

where the specific geometries were generated with GVEC (Hindenlang *et al.* 2019) to be consistent with the background profiles and the prescribed plasma pressures. The reference temperature is $T(x_0) = 4.0$ keV with $x_0/a = 0.5$. The plasma is a hydrogen plasma with realistic electron mass. Together with the reference values of $B_{ref} = 2.28$ T and $L_{ref} = a = 0.52$ m this corresponds to a finite-size parameter $\rho_s^* = \rho_s/a = 1/184$. Furthermore, the radial domain $0.25 \leq x/a \leq 0.75$ was considered, using buffer zones covering 10% of each side of the radial domain. Finally, it should be mentioned that the following simulations exploit the five-fold symmetry of W7-X by only considering one fifth of the toroidal domain.

Linear simulations were performed to compare the growth rates of both scenarios. Since GENE-3D does not use a Fourier representation of the bi-normal direction, all modes are coupled and an initial value calculation will always only resolve the fastest growing mode present in the system. To overcome this issue, one can lower the bi-normal resolution to a point where said mode is no longer resolved, while still properly resolving the magnetic field geometry. While this method is not able to resolve local minima in the linear growth rate spectrum, it serves as a tool to calculate the maximum growth rate present in the system. An alternative is to use a numerical filter to single out the desired mode, as is done, for example, in the EUTERPE code. This is currently not implemented in GENE-3D, but it was shown in Sánchez *et al.* (2021) that both methods are valid approaches. Three simulations were performed for each case, using a resolution of $(120 \times 128 \times 64 \times 24)$ points in $(x, z, v_{||}, \mu)$, with box lengths of size $(L_x, L_y, L_{v_{||}}, L_\mu) = (92.22 \rho_s, 100.64 \rho_s, 4.2 v_{th,\sigma}, 17.7 T_{0,\sigma}(x_0)/B_{ref})$ and hyperdiffusion parameters $\eta_x = \eta_y = 0.05$, $\eta_z = 2.0$ and $\eta_{v_{||}} = 0.2$. The bi-normal resolution was set to $(48, 75, 240)$, respectively, to resolve different linear modes. The corresponding growth rates are shown in figure 7, indicating a clear decrease induced by electromagnetic effects. The precise numerical values are listed in table 2, together with the ratio between the ion and electron heat fluxes, which is used later for comparison with the nonlinear results. One observes a reduction of the growth rates of approximately

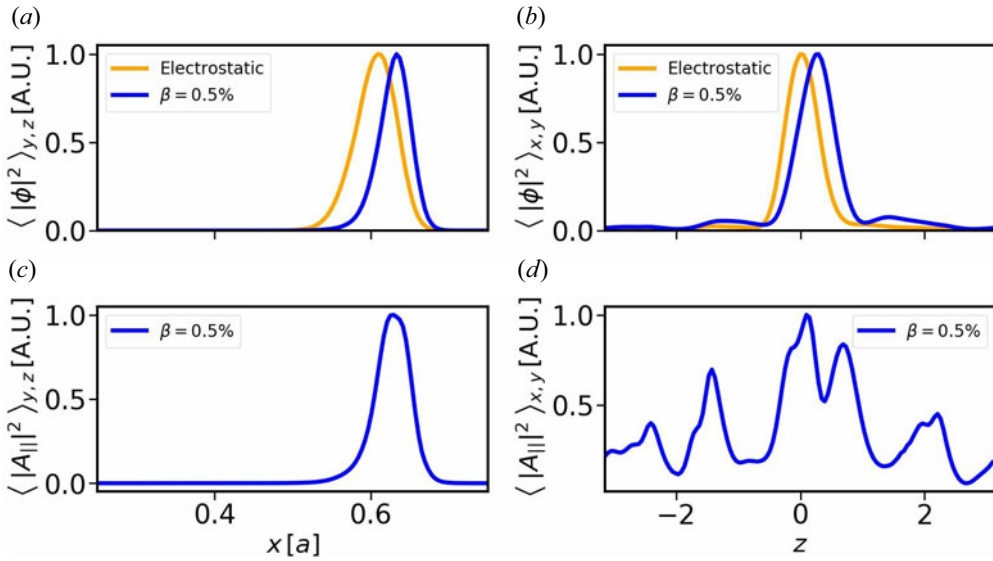


FIGURE 8. Normalised squares of the electrostatic and parallel vector potential of the fastest-growing modes for the electrostatic and electromagnetic scenarios. Radial (a) and poloidal (b) structures of the electrostatic potential, and radial (c) and poloidal (d) structures of the parallel vector potential. The orange lines show the structures of the electrostatic simulation, whereas the blue lines correspond to those of the electromagnetic set-up.

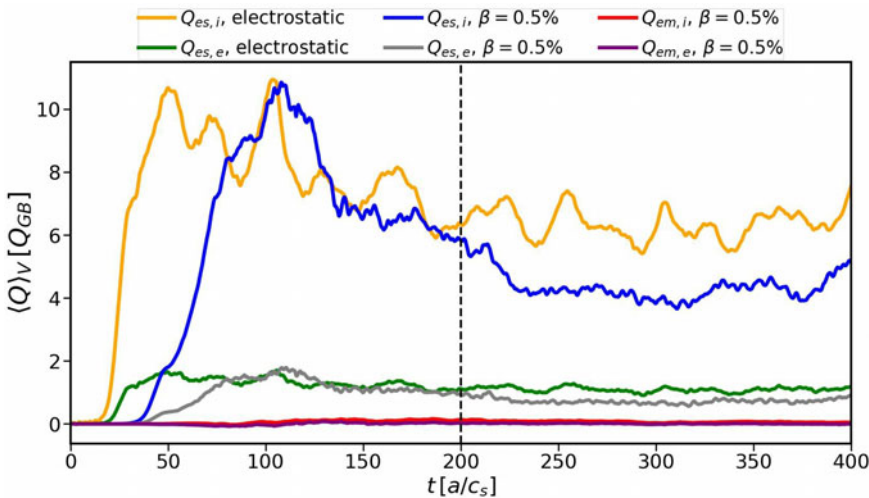


FIGURE 9. Time traces of the volume-averaged heat fluxes; the dashed black line indicates the beginning of the time interval used for averaging.

heat fluxes, as shown in figure 11(a). One can easily see that the total electrostatic heat flux dominates the electromagnetic component with a peak value of $11.99Q_{GB}$, in comparison with the maximum electromagnetic heat flux of $0.36Q_{GB}$. The electrostatic heat flux itself can again be split into contributions coming from the ions and the electrons and can then be compared individually. Figure 11(b) shows the radial profiles of the electrostatic heat fluxes of both scenarios, averaged over a flux surface and in time. The profiles are all

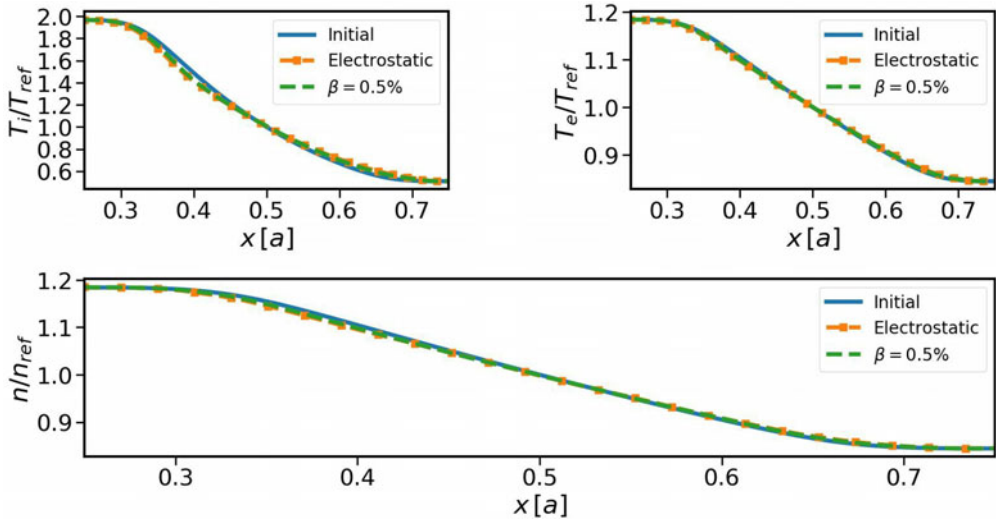


FIGURE 10. Time average of the background density and temperature profiles.

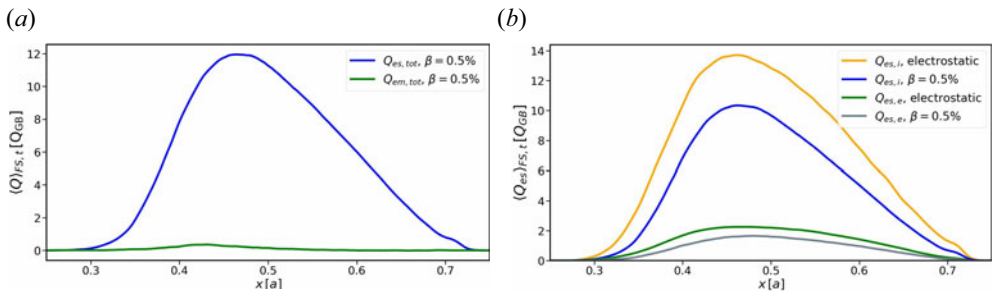


FIGURE 11. Time average of the radial heat flux profiles. (a) Electrostatic and electromagnetic heat fluxes and (b) electrostatic ion and electron heat fluxes.

peaking approximately at $x/a = 0.46$. Both ions and electrons undergo a reduction of their turbulent heat fluxes through electromagnetic effects by approximately 25 %, with the peak ion heat flux being reduced from $13.70Q_{GB}$ to $10.34Q_{GB}$ and the electron flux from $2.25Q_{GB}$ to $1.65Q_{GB}$. One should mention, however, that the aforementioned reduction is observed in gyro-Bohm units only, as the increase in the plasma- β is created by a 50-fold increase in the reference plasma density. This stabilisation is in line with the decrease in linear growth rates shown in table 2. One can further compare the relative magnitudes of ion and electron heat fluxes for both cases to see that they share a common ratio of approximately $Q_{es,e}/Q_{es,i} = 0.15$. This is again similar to what was found in the linear simulations, although there seem to be slight deviations, especially for larger k_y in the electromagnetic simulation.

To understand this, one has to take into account that not all modes contribute equally to turbulence, but that it is rather the low- k_y modes that enter most, in particular for ITG turbulence, as was already shown, for example, in Navarro *et al.* (2020). To confirm this, the bi-normal wave spectra of the electrostatic heat fluxes at $x/a = 0.46$ are shown in figure 12. All the heat fluxes peak around $k_y \rho_s \sim 0.3$, which is below the smallest k_y that was resolved linearly, with only minor contributions from $k_y \rho_s \sim 1$ and beyond.

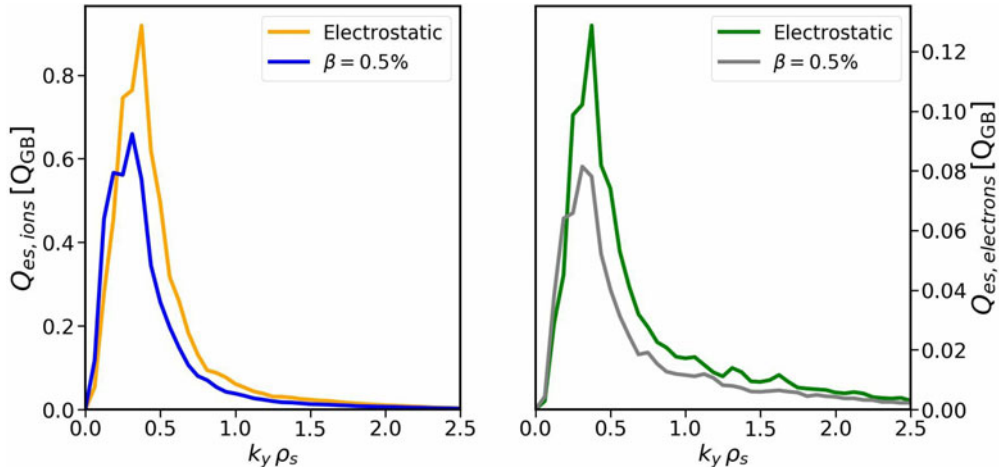


FIGURE 12. Wavenumber spectra of ionic and electronic electrostatic heat fluxes, evaluated at $x/a = 0.46$.

Overall, both linear and nonlinear simulations show a consistent reduction of ITG activity through electromagnetic effects for the given plasma- β . Nevertheless, increasing β will eventually result in the excitation of KBM turbulence, similar to the transition shown in § 3.1, which highlights the importance of electromagnetic effects for future investigations.

5. Conclusion

The present paper focuses on the upgrade of the GENE-3D code to capture electromagnetic effects by retaining a perturbation in the parallel vector potential. The main extension to the numerical scheme of GENE-3D with respect to Maurer *et al.* (2020) was the introduction of an additional field equation to compute the time derivative on the right-hand side of the gyrokinetic equation. Both linear and nonlinear verification studies show excellent agreement with the well-established tokamak code GENE, proving the correct implementation and viability of the electromagnetic upgrade.

The code was then applied to W7-X with the goal of addressing electromagnetic stabilisation of ITG turbulence. To this end, a set of analytical density and temperature profiles was considered in the standard configuration of W7-X. Linear and nonlinear simulations have been performed comparing the results between an electromagnetic case with $\beta_e(x/a) = 0.5\%$ and a case in the electrostatic limit. Electromagnetic effects cause a reduction by 25% of the linear growth rates, which in turn results in a similar reduction of the saturated nonlinear fluxes. While these results were obtained under simplifying assumptions, e.g. using analytical profiles and artificial reference parameters, they demonstrate that GENE-3D is able to perform electromagnetic simulations and that finite- β stabilisation can be important for stellarators as well.

In order to approach such applications without these constraints, realistic simulations of W7-X discharges are planned for the future. Furthermore, it will be of great interest to study electromagnetic instabilities in medium- to high-plasma- β regimes in stellarators.

Acknowledgements

F.W. would like to thank K. Stimmel, T. Hayward-Schneider and D. Michels for many fruitful discussions, helpful suggestions and comments. Numerical simulations were

performed at the MARCONI-Fusion supercomputer at Cineca, Italy, as well as at the Cobra and Raven HPC systems at the Max Planck Computing and Data Facility (MPCDF), Germany.

Editor Per Helander thanks the referees for their advice in evaluating this article.

Funding

This work has been carried out within the framework of the EUROfusion Consortium and has received funding from the Euratom research and training programme 2014–2018 and 2019–2020 under grant agreement no. 633053. The views and opinions expressed herein do not necessarily reflect those of the European Commission.

Declaration of interests

The authors report no conflict of interest.

Appendix A. Additional numerical details

This appendix briefly mentions some additional numerical details of GENE-3D, a detailed discussion of which can be found in Maurer *et al.* (2020).

Phase-space variables are discretised in order to solve the gyrokinetic system numerically. For this, the velocity space parallel to the magnetic field lines is partitioned on an equidistant grid with zero Dirichlet boundaries, whereas the grid in the direction of the magnetic moment is distributed using a Gauss quadrature scheme with Gauss–Legendre weights and knots (Abramowitz & Stegun 1965). For the spatial discretisation, the three field-aligned coordinates

$$\left. \begin{aligned} x &= \rho_{\text{tor}} \\ y &= \sigma_{B_p} C_y \alpha \\ z &= \sigma_{B_p} \theta^* \end{aligned} \right\} \quad (\text{A } 1)$$

are introduced. Here, $\rho_{\text{tor}} = \sqrt{\Phi_{\text{tor}}/\Phi_{\text{edge}}}$ is used as a radial coordinate, where Φ_{tor} is the toroidal flux and Φ_{edge} its value at the last closed flux surface. The bi-normal coordinate y is based on the field line label $\alpha = q(x)\theta^* - \varphi$ at a fixed flux surface, where $q(x)$ is the safety factor, θ^* is the poloidal PEST angle (Li, Breizman & Zheng 2016), φ is the geometrical toroidal angle and the constant C_y is defined as $C_y = x_0/|q_0|$, where q_0 is the safety factor at the reference point x_0 . Lastly, the parallel coordinate z describes the position along a magnetic field line. In addition, the sign of the poloidal magnetic field σ_{B_p} ensures that the parallel direction is always in the direction of the magnetic field. The magnetic field, as well as other geometric coefficients, such as the safety factor profile and metric coefficients, are provided via an interface by the Galerkin Variational Equilibrium Code (GVEC), an ideal magnetohydrodynamics equilibrium solver which follows the ideas of the well-established VMEC code (Hirshman & Whitson 1983; Hirshman & Betancourt 1991).

The spatial grids in GENE-3D themselves are rectangular, equidistant meshes, which makes it particularly easy to calculate spatial derivatives using a fourth-order-accurate central-difference scheme. The boundaries in the radial direction have zero-valued Dirichlet conditions. The bi-normal coordinate is treated periodically, whereas the well-established twist-and-shift boundary condition (Beer *et al.* 1995) is used at the boundaries along a magnetic field line.

In order to avoid unphysical high-wavenumber modes that arise due to the central-difference approximations, one can introduce numerical hyperdiffusion terms to

the right-hand side of the gyrokinetic equation to dampen these modes. The hyperdiffusion terms in the x , y , z and $v_{||}$ directions are all fourth-order-accurate terms with second-order stencils, meaning that they are of the form

$$\mathcal{H}_{u_i} = \eta_u \frac{-F_{1,\sigma}(u_{i-2}) + F_{1,\sigma}(u_{i-1}) - 6F_{1,\sigma}(u_i) + 4F_{1,\sigma}(u_{i+1}) - F_{1,\sigma}(u_{i+2})}{16\Delta u}, \tag{A 2}$$

where u represents any of the previously mentioned coordinates and the damping parameter η_u can be set for each coordinate individually as input by the user.

By applying radial Dirichlet boundary conditions to the distribution functions, density and temperature profiles are fixed at the boundaries of the radial domain, which can cause strong turbulence and numerical instabilities at the boundaries. To avoid this, it is advisable to employ a Krook damping operator of the form

$$K_x = -\nu(x)F_{1,\sigma} \tag{A 3}$$

to the right-hand side of (2.12), where the damping factor $\nu(x)$ is implemented as a fourth-order polynomial with compact support within a buffer region at the radial boundaries, typically 5%–10% at each side of the domain (Görlner *et al.* 2011). As GENE-3D uses a gradient-driven approach (Görlner *et al.* 2011; Rath *et al.* 2016; Lanti *et al.* 2018) so far, numerical particle and heat sources have to be introduced to the gyrokinetic equation (2.12) in order to maintain the density and temperature profiles. The sources are of the form

$$S_{P,\sigma} = -\kappa_P \frac{\langle F_{M,\sigma}(\mathbf{X}, |v_{||}|, \mu) \rangle_{\text{FS}}}{\sum_{\sigma} \left\langle \int F_{M,\sigma}(\mathbf{X}, |v_{||}|, \mu) d^3v \right\rangle_{\text{FS}}} \sum_{\sigma} \left\langle \int \langle F_{1,\sigma}(\mathbf{X}, |v_{||}|, \mu) \rangle_{\text{FS}} d^3v \right\rangle_{\text{FS}} \tag{A 4}$$

in the case of the particle source and

$$S_{H,\sigma} = -\kappa_H \left[\langle F_{1,\sigma}(\mathbf{X}, |v_{||}|, \mu) \rangle_{\text{FS}} - \frac{\left\langle \int \langle F_{1,\sigma}(\mathbf{X}, |v_{||}|, \mu) \rangle_{\text{FS}} d^3v \right\rangle_{\text{FS}}}{\left\langle \int \langle F_{M,\sigma}(\mathbf{X}, |v_{||}|, \mu) \rangle_{\text{FS}} d^3v \right\rangle_{\text{FS}}} \langle F_{M,\sigma}(\mathbf{X}, |v_{||}|, \mu) \rangle_{\text{FS}} \right] \tag{A 5}$$

for the heat source. Here,

$$\langle \cdot \rangle_{\text{FS}} = \frac{\partial}{\partial V} \int_V \cdot dV' \tag{A 6}$$

denotes the flux-surface average (D’haeseleer *et al.* 2012) and

$$F_{1,\sigma}(\mathbf{X}, |v_{||}|, \mu) = \frac{F_{1,\sigma}(\mathbf{X}, v_{||}, \mu) + F_{1,\sigma}(\mathbf{X}, -v_{||}, \mu)}{2}. \tag{A 7}$$

The symmetrisation of the distribution function with respect to $v_{||}$ in (A5) ensures the conservation of parallel momentum and the terms proportional to $\langle \int \dots \rangle_{\text{FS}} / \langle \int \dots \rangle_{\text{FS}}$ avoids the unwanted numerical injection of particles (McMillan *et al.* 2008). The coefficients κ_P and κ_H are specified by the user and should be chosen to be around 5%–10% of the maximum linear growth rate of the system (Lapillonne *et al.* 2010).

The nonlinear term in (2.13), coupling \mathbf{v}_χ to $F_{1,\sigma}$ and ϕ_1 , can be written in the form

$$\begin{aligned}
 & -\mathbf{v}_\chi \cdot \left(\nabla F_{1,\sigma} + \frac{q_\sigma F_{M,\sigma}}{T_{0,\sigma}} \nabla \mathcal{G}\{\phi_1\} \right) \\
 &= \frac{c}{B_0} (\mathbf{b}_0 \times \nabla \mathcal{G}\{\chi\}) \cdot \left(\nabla F_{1,\sigma} + \frac{q_\sigma F_{M,\sigma}}{T_{0,\sigma}} \nabla \mathcal{G}\{\phi_1\} \right) \\
 &= \frac{c}{B_0} \left[\mathbf{b}_0 \cdot (\nabla F_{1,\sigma} \times \nabla \mathcal{G}\{\chi\}) + \frac{q_\sigma F_{M,\sigma}}{T_{0,\sigma}} \mathbf{b}_0 \cdot (\nabla \mathcal{G}\{\phi_1\} \times \nabla \mathcal{G}\{\chi\}) \right] \\
 &= \frac{c}{B_0} \left[\{F_{1,\sigma}, \mathcal{G}\{\chi\}\}_{x,y} + \frac{q_\sigma F_{M,\sigma}}{T_{0,\sigma}} \{\mathcal{G}\{\phi_1\}, \mathcal{G}\{\chi\}\}_{x,y} \right], \tag{A 8}
 \end{aligned}$$

where the two-dimensional Poisson brackets for functions A and B have been defined here as

$$\{A, B\}_{x,y} = \frac{\partial A}{\partial x} \frac{\partial B}{\partial y} - \frac{\partial B}{\partial x} \frac{\partial A}{\partial y}. \tag{A 9}$$

An Arakawa scheme (Arakawa 1997) is used to evaluate the Poisson brackets in (A8) numerically, as it ensures the conservation of free energy in nonlinear simulations (Bañón Navarro *et al.* 2011).

Finally, in order to perform the gyroaverages efficiently, the distribution functions as well as the electromagnetic fields are discretised using a finite-element method in the directions perpendicular to the magnetic field, currently employing bicubic piecewise polynomials. Doing so, together with the finite-difference approximations of the derivatives, allows one to transform the field equations (2.9), (2.10) and (2.15) into a set of sparse, linear systems. This makes it possible to use the PETSc library (Balay *et al.* 1997, 2019) in order to solve the equations for the electromagnetic fields. While providing an extensive set of iterative solvers already, PETSc can also serve as an interface to direct solvers such as MUMPS (Amestoy *et al.* 2001, 2006) or SuperLU_ (Li & Demmel 2003).

REFERENCES

- ABRAMOWITZ, M. & STEGUN, I.A. 1965 Handbook of mathematical functions with formulas, graphs, and mathematical table. In *US Department of Commerce* (ed. M. Abramowitz & I.A. Stegun). National Bureau of Standards Applied Mathematics series 55.
- AMESTOY, P.R., DUFF, I.S., L'EXCELLENT, J.-Y. & KOSTER, J. 2001 A fully asynchronous multifrontal solver using distributed dynamic scheduling. *SIAM J. Matrix Anal. Applics.* **23** (1), 15–41.
- AMESTOY, P.R., GUERMOUCHE, A., L'EXCELLENT, J.-Y. & PRALET, S. 2006 Hybrid scheduling for the parallel solution of linear systems. *Parallel Comput.* **32** (2), 136–156.
- ARAKAWA, A. 1997 Computational design for long-term numerical integration of the equations of fluid motion: two-dimensional incompressible flow. Part I. *J. Comput. Phys.* **135** (2), 103–114.
- BALAY, S., ABHYANKAR, S., ADAMS, M.F., BROWN, J., BRUNE, P., BUSCHELMAN, K., DALCIN, L., EIJKHOUT, V., GROPP, W.D., KARPEYEV, D., *et al.* 2019 PETSc users manual. *Tech. Rep.* ANL-95/11 – Revision 3.11. Argonne National Laboratory.
- BALAY, S., GROPP, W.D., MCINNES, L.C. & SMITH, B.F. 1997 Efficient management of parallelism in object oriented numerical software libraries. In *Modern Software Tools in Scientific Computing* (ed. E. Arge, A.M. Bruaset & H.P. Langtangen), pp. 163–202. Birkhäuser Press.
- BAÑÓN NAVARRO, A., MOREL, P., ALBRECHT-MARC, M., CARATI, D., MERZ, F., GÖRLER, T. & JENKO, F. 2011 Free energy balance in gyrokinetic turbulence. *Phys. Plasmas* **18** (9), 092303.
- BEER, M.A., COWLEY, S.C. & HAMMETT, G.W. 1995 Field-aligned coordinates for nonlinear simulations of tokamak turbulence. *Phys. Plasmas* **2** (7), 2687–2700.

- BRIZARD, A.J. & HAHM, T.S. 2007 Foundations of nonlinear gyrokinetic theory. *Rev. Mod. Phys.* **79** (2), 421.
- COLE, M.D.J., MORITAKA, T., HAGER, R., DOMINSKI, J., KU, S. & CHANG, C.S. 2020 Nonlinear global gyrokinetic delta- f turbulence simulations in a quasi-axisymmetric stellarator. *Phys. Plasmas* **27** (4), 044501.
- CRANDALL, P. 2019 Collisional and electromagnetic physics in gyrokinetic models. PhD thesis, UCLA.
- D'HAESELEER, W.D., HITCHON, W.N.G., CALLEN, J.D. & SHOHEET, J.L. 2012 *Flux Coordinates and Magnetic Field Structure: A Guide to a Fundamental Tool of Plasma Theory*. Springer Science & Business Media.
- GARBET, X., IDOMURA, Y., VILLARD, L. & WATANABE, T.H. 2010 Gyrokinetic simulations of turbulent transport. *Nucl. Fusion* **50** (4), 043002.
- GÖRLER, T., LAPILLONNE, X., BRUNNER, S., DANNERT, T., JENKO, F., AGHDAM, S.K., MARCUS, P., MCMILLAN, B.F., MERZ, F., SAUTER, O., *et al.* 2011 Flux-and gradient-driven global gyrokinetic simulation of tokamak turbulence. *Phys. Plasmas* **18** (5), 056103.
- GÖRLER, T., LAPILLONNE, X., BRUNNER, S., DANNERT, T., JENKO, F., MERZ, F. & TOLD, D. 2011 The global version of the gyrokinetic turbulence code gene. *J. Comput. Phys.* **230** (18), 7053–7071.
- GÖRLER, T., TRONKO, N., HORNSBY, W.A., BOTTINO, A., KLEIBER, R., NORSCINI, C., GRANDGIRARD, V., JENKO, F. & SONNENDRÜCKER, E. 2016 Intercode comparison of gyrokinetic global electromagnetic modes. *Phys. Plasmas* **23** (7), 072503.
- HELANDER, P. & SIMAKOV, A.N. 2008 Intrinsic ambipolarity and rotation in stellarators. *Phys. Rev. Lett.* **101**, 145003.
- HINDENLANG, F., MAJ, O., STRUMBERGER, E., RAMPP, M. & SONNENDRÜCKER, E. 2019 GVEC: a newly developed 3D ideal MHD Galerkin variational equilibrium code, Presentation given in 'Simmons Collaboration on Hidden Symmetries in Fusion Energy'.
- HIRSHMAN, S.P. & BETANCOURT, O. 1991 Preconditioned descent algorithm for rapid calculations of magnetohydrodynamic equilibria. *J. Comput. Phys.* **96** (1), 99–109.
- HIRSHMAN, S.P. & WHITSON, J.C. 1983 Steepest-descent moment method for three-dimensional magnetohydrodynamic equilibria. *Phys. Fluids* **26** (12), 3553–3568.
- JENKO, F., DORLAND, W., KOTSCHENREUTHER, M. & ROGERS, B.N. 2000 Electron temperature gradient driven turbulence. *Phys. Plasmas* **7** (5), 1904–1910.
- KLINGER, T., ANDREEVA, T., BOZHENKOV, S., BRANDT, C., BURHENN, R., BUTTENSCHÖN, B., FUCHERT, G., GEIGER, B., GRULKE, O., LAQUA, H.P., *et al.* 2019 Overview of first wendelstein 7-x high-performance operation. *Nucl. Fusion* **59** (11), 112004.
- LANTI, E., MCMILLAN, B.F., BRUNNER, S., OHANA, N. & VILLARD, L. 2018 Gradient-and flux-driven global gyrokinetic simulations of ITG and TEM turbulence with an improved hybrid kinetic electron model. In *Journal of Physics: Conference Series*, vol. 1125, p. 012014. IOP Publishing Ltd.
- LAPILLONNE, X., MCMILLAN, B.F., GÖRLER, T., BRUNNER, S., DANNERT, T., JENKO, F., MERZ, F. & VILLARD, L. 2010 Nonlinear quasisteady state benchmark of global gyrokinetic codes. *Phys. Plasmas* **17** (11), 112321.
- LI, M., BREIZMAN, B.N. & ZHENG, L. 2016 Canonical straight field line magnetic flux coordinates for tokamaks. *J. Comput. Phys.* **326**, 334–341.
- LI, X.S. & DEMMEL, J.W. 2003 SuperLU_DIST: a scalable distributed-memory sparse direct solver for unsymmetric linear systems. *ACM Trans. Math. Softw.* **29** (2), 110–140.
- MAURER, M., NAVARRO, A.B., DANNERT, T., RESTELLI, M., HINDENLANG, F., GÖRLER, T., TOLD, D., JAREMA, D., MERLO, G. & JENKO, F. 2020 GENE-3D: a global gyrokinetic turbulence code for stellarators. *J. Comput. Phys.* **420**, 109694.
- MCMILLAN, B.F., JOLLIET, S., TRAN, T.M., VILLARD, L., BOTTINO, A. & ANGELINO, P. 2008 Long global gyrokinetic simulations: source terms and particle noise control. *Phys. Plasmas* **15** (5), 052308.
- MISHCHENKO, A. & KLEIBER, R. 2012 Zonal flows in stellarators in an ambient radial electric field. *Phys. Plasmas* **19** (7), 072316.
- NAVARRO, A.B., MERLO, G., PLUNK, G.G., XANTHOPOULOS, P., VON STECHOW, A., DI SIENA, A., MAURER, M., HINDENLANG, F., WILMS, F. & JENKO, F. 2020 Global gyrokinetic simulations of

- ITG turbulence in the magnetic configuration space of the wendelstein 7-x stellarator. *Plasma Phys. Control. Fusion* **62** (10), 105005.
- OBERPARLEITER, M., JENKO, F., TOLD, D., DOERK, H. & GÖRLER, T. 2016 Interaction between neoclassical effects and ion temperature gradient turbulence in gradient-and flux-driven gyrokinetic simulations. *Phys. Plasmas* **23** (4), 042509.
- RATH, F., PEETERS, A.G., BUCHHOLZ, R., GROSSHAUSER, S.R., MIGLIANO, P., WEIKL, A. & STRINTZI, D. 2016 Comparison of gradient and flux driven gyro-kinetic turbulent transport. *Phys. Plasmas* **23** (5), 052309.
- REYNDERS, J.V.W. 1993 Gyrokinetic simulation of finite-beta plasmas on parallel architectures. PhD thesis, Princeton University.
- SÁNCHEZ, E., GARCÍA-REGAÑA, J.M., NAVARRO, A.B., PROLL, J.H.E., MORENO, C.M., GONZÁLEZ-JEREZ, A., CALVO, I., KLEIBER, R., RIEMANN, J., SMONIEWSKI, J., *et al.* 2021 Gyrokinetic simulations in stellarators using different computational domains. [arXiv:2106.02828](https://arxiv.org/abs/2106.02828).
- SÁNCHEZ, E., MISHCHENKO, A., GARCÍA-REGAÑA, J.M., KLEIBER, R., BOTTINO, A., VILLARD, L. & THE W7-X TEAM 2020 Nonlinear gyrokinetic PIC simulations in stellarators with the code EUTERPE. [arXiv:2004.14605](https://arxiv.org/abs/2004.14605).
- SNYDER, P.B. & HAMMETT, G.W. 2001 Electromagnetic effects on plasma microturbulence and transport. *Phys. Plasmas* **8** (3), 744–749.
- WANG, H.Y., HOLOD, I., LIN, Z., BAO, J., FU, J.Y., LIU, P.F., NICOLAU, J.H., SPONG, D. & XIAO, Y. 2020 Global gyrokinetic particle simulations of microturbulence in w7-x and LHD stellarators. *Phys. Plasmas* **27** (8), 082305.
- WOLF, R.C. & THE WENDELSTEIN 7-X TEAM 2008 A stellarator reactor based on the optimization criteria of wendelstein 7-x. *Fusion Engng Des.* **83** (7–9), 990–996.